

1
2
3
4
5
6
7
8
9
10
11
12
13
14
15
16
17
18
19
20
21
22
23
24
25
26
27
28
29
30
31
32
33
34
35
36
37
38
39
40
41

The formation and chronology of the PAT 91501 impact-melt L-chondrite with vesicle-metal-sulfide assemblages

G.K. Benedix¹, R.A. Ketcham², L. Wilson³, T.J. McCoy⁴, D.D. Bogard⁵, D.H. Garrison⁶,
G.F. Herzog⁷, S. Xue⁷, J. Klein⁸, and R. Middleton^{8,*}

¹Impact and Astromaterials Research Centre (IARC)/Department of Mineralogy, The Natural History Museum, Cromwell Road, London, SW7 5BD UK
(g.benedix@nhm.ac.uk)

²Dept. of Geological Sciences, Jackson School of Geosciences, Univ. of Texas at Austin, Austin, TX 78712 USA

³Environmental Sci. Dept., Lancaster Univ., Lancaster LA1 4YQ UK.

⁴Dept. of Mineral Sciences, National Museum of Natural History, Smithsonian Institution, Washington, DC 20560-0119 USA

⁵ARES, NASA-JSC, Houston TX 77058

⁶ESCG/Barrios Technology, Houston, TX 77058

⁷Rutgers Univ., Piscataway, NJ 08854-8087

⁸Univ. Pennsylvania, Philadelphia, PA 19104.

For submission to *Geochimica et Cosmochimica Acta*

**Deceased*

41 **Abstract** – The L chondrite Patuxent Range (PAT) 91501 is an 8.5-kg unshocked,
42 homogeneous, igneous-textured impact melt that cooled slowly compared to other
43 meteoritic impact melts in a crater floor melt sheet or sub-crater dike (Mittlefehldt and
44 Lindstrom, 2001). We conducted mineralogical and tomographic studies of previously
45 unstudied mm- to cm-sized metal-sulfide-vesicle assemblages and chronologic studies of
46 the silicate host. Metal-sulfide clasts constitute about 1 vol.%, comprise zoned taenite,
47 troilite and pentlandite, and exhibit a consistent orientation between metal and sulfide and
48 of metal-sulfide contacts. Vesicles make up ~2 vol.% and exhibit a similar orientation of
49 long axes. ^{39}Ar - ^{40}Ar measurements date the time of impact at 4.461 ± 0.008 Gyr B.P.
50 Cosmogenic noble gases and ^{10}Be and ^{26}Al activities suggest a pre-atmospheric radius of
51 40-60 cm and a cosmic ray exposure age of 25-29 Myr, similar to ages of a cluster of L
52 chondrites. PAT 91501 dates the oldest known impact on the L chondrite parent body.
53 The dominant vesicle-forming gas was S_2 (~15-20 ppm), which formed in equilibrium
54 with impact-melted sulfides. The meteorite formed in an impact melt dike beneath a
55 crater, as did other impact melted L chondrites, such as Chico. Cooling and solidification
56 occurred over ~2 hours. During this time, ~90% of metal and sulfide segregated from the
57 local melt. Remaining metal and sulfide grains oriented themselves in the local
58 gravitational field, a feature nearly unique among meteorites. Many of these metal-
59 sulfide grains adhered to vesicles to form aggregates that may have been close to
60 neutrally buoyant. These aggregates would have been carried upward with the residual
61 melt, inhibiting further buoyancy-driven segregation. Although similar processes
62 operated individually in other chondritic impact melts, their interaction produced the
63 unique assemblage observed in PAT 91501.

64

64

1. INTRODUCTION

65 Impact is one of three fundamental processes, along with accretion and
66 differentiation, which formed and modified asteroid bodies. From nebular accretion
67 through to modern times, impact has left its traces in the ubiquitous cratered surfaces,
68 distorted shapes, and telltale signs of shocked minerals and melts recorded in meteorites.
69 Despite this abundant evidence, our knowledge of the physical processes and the timing
70 of impact on asteroidal bodies remains incomplete. While we have many well-
71 documented impact craters on Earth to serve as our guide to interpreting impact
72 phenomena on other planets, we have only random sampling of asteroidal impact craters.
73 Further, our knowledge of chronology is limited because the samples we do have may not
74 accurately reflect the impact flux throughout the history of the Solar System. Continuing
75 study of impact-derived meteorites can help fill these gaps in our knowledge.

76 Melt veined meteorites, impact melt breccias, and impact melts are not
77 uncommon among the known ordinary chondrite population. They have been studied
78 extensively to understand their origin (Rubin, 1985; Stöffler et al., 1991). In particular,
79 considerable effort has focused on relating these meteorites to the physical setting of their
80 formation, starting with the location of their melt. Melt can form on the floor and walls of
81 a crater or in subsurface dikes that may extend beyond its walls. Each of these settings
82 provides a unique physical and thermal environment for the incorporation of clastic
83 material and cooling history.

84 Impact rates were much higher in the early history of the solar system (Hartmann
85 et al., 2000), but those impacts are probably recorded in the asteroid belt by the
86 population of small bodies produced by the break-up of larger precursor asteroids.

87 Impact craters observed on asteroids today are more recent events, consistent with the
88 fact that most strong impact events in chondrites occurred within the past 1 Gyr, as
89 determined by Ar-Ar radiometric dating (Bogard, 1995, and references therein). For
90 example, many L-chondrites show Ar-Ar impact heating ages clustering near 0.5 Gyr,
91 perhaps dating the time of disruption of the parent body (Haack et al., 1996).
92 Interestingly, chronological evidence for collisional events very early in asteroid history
93 is sparse.

94 This paper presents a multidisciplinary study of PAT 91501, a vesicular, impact
95 melted L chondrite (Score and Lindstrom, 1992). Vesicles have been reported in only
96 two other ordinary chondrite impact melts: Shaw (Taylor et al., 1979) and Cat Mountain
97 (Kring et al., 1996). Although these meteorites are chemically and petrologically well-
98 characterized (Harvey and Roeder, 1994, Mittlefehldt and Lindstrom, 2001), no study has
99 addressed the implications of the presence of vesicles in impact melt rocks. Our
100 objectives were to document the meteorite's impact and cosmic ray exposure history and
101 to understand the genesis of the unusual vesicular nature of this meteorite.

102 **2. SAMPLES AND ANALYTICAL TECHNIQUES**

103 Patuxent Range (PAT) 91501 was recovered in Antarctica during the 1991-1992
104 collecting season. It was transported more than 800 m prior to cataloging (R.P. Harvey,
105 pers. comm.). Numerous large and small pieces, totaling more than 8.5 kg, were
106 collected. Their relative positions in the meteoroid are unknown. In the same locale, two
107 small metal-sulfide nodules (PAT 91516 and 91528; Clarke, 1994) were recovered. As
108 discussed below, these meteorites are petrologically identical to metal-sulfide nodules

109 from PAT 95101 and are almost certainly samples from the same original mass (R.P.
110 Harvey, pers. comm.).

111 PAT 91501 was originally classified as an L7 chondrite (Score and Lindstrom,
112 1992) based on textural features, mineral chemistry and oxygen isotopic composition,
113 although it was noted that it was similar in many respects to the Shaw L chondrite impact
114 melt. On further investigation (Harvey and Roedder, 1994; Mittlefehldt and Lindstrom,
115 2001), it was determined to be a near-total impact melt of an L chondrite.

116 One of the most striking features of PAT 91501 is the mm- to cm-sized vesicles
117 seen on cut surfaces of the sample (Fig. 1), as originally noted by Marlow et al. (1992).
118 We focused on PAT 91501 because it contains large vesicles that are visible in hand
119 sample (Fig. 1), there is abundant material, and it has been described as a total impact
120 melt (Mittlefehldt and Lindstrom, 2001). Visual inspection of PAT 91501 ,50 (2814.3 g)
121 and ,78 (127.6 g) show clastless, light colored surfaces with cm-sized vesicles and
122 metal/troilite aggregates.

123 **2.1 Petrology**

124 All available thin sections of PAT 91501 (,26; ,27; ,28; ,95; and ,111) at the
125 Smithsonian National Museum Natural History, as well as sections of PAT 91516 and
126 PAT 91528, were examined in both reflected and transmitted light with an optical
127 microscope. Metal and troilite compositions were analyzed using a JEOL JXA 8900R
128 electron microprobe at the Smithsonian. Analytical conditions were 20kV and 20nA.
129 Well-known standards were used and analyses were corrected using a manufacturer
130 supplied ZAF correction routine. Sulfur isotopes were analyzed using the 6f ion

131 microprobe at the Carnegie Institution of Washington utilizing Canyon Diablo troilite as
132 the standard.

133 The two hand samples described above (,50 and ,78) were imaged at the High
134 Resolution X-ray Computed Tomography facility at the University of Texas at Austin
135 (UTCT), which is described in detail by Ketcham and Carlson (2001). The focus of our
136 work was to determine the distribution of vesicles, metal and sulfide, which are easily
137 distinguished based on their large density contrast from the silicate matrix. Sample PAT
138 91501 ,50 was scanned using the high-energy subsystem, with X-rays set at 420 kV and
139 4.7 mA, with a focal spot size of 1.8 mm. The samples were scanned in air and, to reduce
140 scan artifacts, the beam was pre-filtered with 1.58 mm of brass. Each slice was
141 reconstructed from 1800 views, with an acquisition time of 128 ms per view. A total of
142 141 (1024x1024) slices were acquired with a thickness and spacing of 0.5 mm, imaging a
143 196 mm field of view. The final scan images were post-processed for ring artifact
144 removal. Sample PAT 91501,78 was imaged using the microfocal subsystem, with X-
145 rays at 180 kV and 0.25 mA, and a focal spot size of approximately 0.05 mm. The
146 sample was sealed and placed in a cylinder and surrounded by water, which was used as a
147 wedge calibration to reduce scan artifacts. Data for 31 slice images were acquired during
148 each rotation of the sample; over each rotation, 1000 views were acquired with an
149 acquisition time of 267 ms per view. A total of 927 (1024x1024) slices at 0.0726 mm
150 intervals, each showing a 67 mm field of view, were acquired. Scans were reconstructed
151 using a software correction to further reduce beam hardening artifacts. Animations,
152 including flipbooks for the 2D computed tomography scans and 3D rotational renderings
153 are available at UTCT. (Movie and flipbook of PAT 91501,50 can be seen at
<http://web.mac.com/metritedoc/>

154 Measurements of vesicles and metal/troilite particles from the CT data volume
155 were made using Blob3D software (Ketcham, 2005), and visualizations were made using
156 Amira® version 3.1.

157 **2.2 Chronology (³⁹Ar-⁴⁰Ar ages and cosmic-ray exposure ages)**

158 A 48-mg whole rock sample of PAT91501 ,109 was irradiated with fast neutrons,
159 along with multiple samples of the NL-25 hornblende age standard. This irradiation
160 converted a portion of the ³⁹K into ³⁹Ar, and the ⁴⁰Ar/³⁹Ar ratio is proportional to the K-
161 Ar age. The irradiation constant (J-value) was 0.025210 ±0.000125. Ar was released
162 from PAT 91501 in 34 stepwise temperature extractions and its isotopic composition was
163 measured on a mass spectrometer. Experimental details are given in Bogard et al. (1995).
164 Two unirradiated whole rock samples of PAT 91501, taken from different locations in the
165 meteorite (see below), were degassed in either two or four stepwise temperature
166 extractions and the He, Ne, and Ar released were analyzed on a mass spectrometer. All
167 noble gas analyses were made at NASA-JSC.

168 We analyzed chips from four different specimens (subsamples 34, 38, 40, and 42)
169 of PAT 91501. Sample ,34 was located adjacent to sample ,106, which was analyzed for
170 noble gases. Using facilities at Rutgers, the four specimens were ground and weighed.
171 After addition of Al and Be carriers, the powders were dissolved in strong mineral acids.
172 Beryllium and aluminum were separated by ion exchange, precipitated as the hydroxides,
173 and ignited to the oxides as described by Vogt and Herpers (1988). The activities of ¹⁰Be
174 and ²⁶Al were measured by accelerator mass spectrometry at the University of
175 Pennsylvania as described by Middleton and Klein (1986) and Middleton et al. (1983)

176 (Table 1). As the ^{10}Be activity of sample ,40 was unaccountably low and inconsistent
177 with the ^{26}Al activity, we do not report it.

178

3. PREVIOUS WORK

179 The petrology of the silicate portion of PAT 91501 is reported by Harvey and
180 Roedder (1994) and Mittlefehldt and Lindstrom (2001) and we briefly review this work.
181 PAT 91501 is an unshocked, homogeneous, igneous-textured rock of broadly L chondrite
182 mineralogy and chemistry. Major element mineral chemistries were shown to be
183 consistent with those of L chondrite; the minor element chemistry of olivine and low-Ca
184 pyroxene, on the other hand, is consistent with melting (Mittlefehldt and Lindstrom,
185 2001); depletions of Zn and Br and sequestration of siderophile and chalcophile elements
186 into the large, heterogeneously-distributed metal-sulfide aggregates were observed
187 (Mittlefehldt and Lindstrom, 2001). Relic material includes rare chondrules, as well as
188 opaque-inclusion-rich olivine and some low-Ca pyroxene grains that comprise ~10 vol.%
189 of the meteorite, but distinct clasts commonly found in impact melt breccias are absent.
190 Mittlefehldt and Lindstrom (2001) concluded that PAT 91501 is an impact melt of an L
191 chondrite that crystallized at a cooling rate slower than that typical for impacts melts and
192 likely formed in a melt sheet on the crater floor or in a sub-crater melt dike.

193

4. RESULTS

194 We report our analyses of the metal-sulfide-vesicle assemblages, based on both
195 microscopic examination and computed tomography, and the results of the chronological
196 analyses for both ^{39}Ar - ^{40}Ar and cosmogenic noble gases and radionuclides.

197 4.1 Petrography of metal-sulfide assemblages

198 PAT 91501 contains both vesicles and rounded metal-sulfide nodules that reach 1
199 cm in diameter. Previous studies have focused primarily on the silicate portion (Harvey
200 and Roedder, 1994; Mittlefehldt and Lindstrom, 2001), with neither study reporting
201 detailed examination of a metal-sulfide nodule in thin section. As we discuss later,
202 metal-sulfide nodules are rare, with less than 1 per cm³. Apart from a single chemical
203 analysis of troilite reported by Mittlefehldt and Lindstrom (2001), they have never been
204 studied from PAT 91501.

205 We examined a 5-mm-diameter metal-sulfide nodule adjacent to a 5-mm-diameter
206 vesicle in subsample ,111. This nodule consists of a core of Fe,Ni metal (2 by 3.5 mm)
207 rimmed by sulfide, with the two phases exhibiting numerous mutual protrusions into each
208 other. The sulfide is dominantly troilite, although minor (<1 vol.% of the sulfide)
209 pentlandite ((Fe_{6.15}Ni_{2.62}Co_{0.10})_{Σ=8.88}S₈) is observed at troilite-metal, troilite-silicate and
210 troilite-vesicle boundaries. Schreibersite rims are often found at the border between
211 metal and troilite/pentlandite. The S isotopic composition of pentlandite (3 analyses yield
212 δ³⁴S of 0.5-1.9‰) and troilite (7 analyses yield δ³⁴S of 0.4-1.2‰) are essentially
213 identical. No polycrystallinity or twinning is observed in the troilite, confirming the
214 observation of Mittlefehldt and Lindstrom (2001) that PAT 91501 experienced minimal
215 secondary shock after its crystallization. The metal is composed of two domains (Fig.
216 2a). Rimming each domain is a 50 μm thick region of high-Ni (up to 45 wt.%; Fig. 2b)
217 taenite that is relatively inclusion free. Adjacent to this, Ni decreases systematically from
218 ~40 wt.% to ~20 wt.% and this zoned metal often contains 10-30 μm troilite and 1-5 μm
219 schreibersite inclusions. The center of the largest domain, which appears to have been

220 bisected, is martensitic, with irregular Ni concentrations of 20-25 wt.%, and contains
221 troilite and schreibersite inclusions that can reach tens of microns.

222 While metal-sulfide nodules from PAT 91501 have not been previously described,
223 the published descriptions (Clarke, 1994) for the small iron meteorites PAT 91516 (1.58
224 g) and PAT 91528 (3.34 g) are essentially identical to that given here for PAT 91501.
225 The only substantive difference is that Clarke observed a larger number of metal
226 domains, particularly in PAT 91516, and these were often separated by sinuous troilite.

227 **4.2 Computed Tomography**

228 We used computed tomography (CT) to survey the distribution of vesicles, metal
229 and sulfide in two samples of PAT 91501 (see flipbooks in supplemental data). Figure 3
230 is a single frame of a 3 dimensional, rotational visualization made from the CT scan of
231 PAT 91501 ,50, in which vesicles and metal-sulfide intergrowths are highlighted. In this
232 sample, 5085 vesicles were measured, which comprise ~2 volume percent of the sample.
233 The sizes of the vesicles range in diameter from 0.6 to 14 mm. In contrast, analysis of
234 PAT 91501 ,78 yielded 36685 vesicles ranging in size from 0.2 to ~6mm in diameter.
235 The difference in the numbers and the size range of vesicles is due to the fact that the
236 smaller sample was scanned at a much higher resolution. In both samples, tiny vesicles
237 (<1mm diameter) dominate the population. Vesicles in both samples are homogeneously
238 distributed and have a median aspect ratio of 1.4, indicating moderate elongation.

239 The CT scans revealed the existence and distribution of several large metal-
240 sulfide intergrowths (Fig. 3). Together, metal and sulfide represent less than 1 volume
241 percent of the sample. We measured 255 and 142 metal grains in sample ,50 and ,78,
242 respectively. Metal ranges in size from 0.7 to 8.6 mm in the larger sample and comprises

243 0.27 vol%, while in the smaller sample metal ranges from 0.1 to 3.8 mm and represents
244 0.35 vol%; as with the vesicles, the higher-resolution scan of the smaller sample
245 permitted us to measure particles too small to be resolved in the scan of the larger
246 specimen. Sulfide is more abundant than metal in both samples and occupies
247 approximately twice the volume as metal. Sulfide accounts for 0.4 vol% in the larger
248 sample (,50) and for 0.56 vol% in the smaller sample. We measured 404 sulfide grains in
249 sample ,50 and 540 grains in sample ,78. Sulfide is overall larger than metal and ranges
250 from 0.6 to 12.7mm in ,50 and from 0.2 to 4.7mm in ,78. As with vesicles, tiny grains (<
251 1mm) comprise the mode of both the metal and sulfide size distributions (see flipbooks
252 and 3D renderings in supplemental data).

253 PAT 91501 (,50) contains 169 grains in which metal and sulfide are in contact.
254 These particles were noted by earlier workers (Score and Lindstrom, 1992; Mittlefehldt
255 and Lindstrom, 2001) and attributed to formation as immiscible melts prior to silicate
256 crystallization. Interestingly, these particles exhibit a consistent orientation of the metal
257 and sulfide relative to each other and to the meteorite as a whole. Figure 4a is a stereo
258 plot of the normals to the planes defined by the contact between metal and sulfide with
259 the size of the each circle proportional to the area of the contact. Although some scatter
260 is observed in this plot, particularly for smaller metal-sulfide pairs, the majority of larger
261 particles defines a tight cluster trending 255° and plunging 45° ; note that these
262 orientations are with respect to the scan data, and are not geographical.

263 The CT scans also document the relationship between vesicles, metal, and sulfide.
264 Larger vesicles appear to have metal-sulfide intergrowths associated with them. In the
265 CT scan of the larger sample of PAT 91501, we found 18 instances where vesicles are in

266 contact with metal only, sulfide only or metal-sulfide intergrowths. In the higher
267 resolution CT scan of PAT 91501, 78, there are nearly 200 vesicles in contact with metal,
268 sulfide or metal-sulfide. The vast majority of the largest vesicles are in contact with
269 metal and/or sulfide.

270 The elongation of vesicles allows us to examine their orientation as well. Fig. 4b
271 is a stereo plot of the orientations of the vesicle long axes from the main mass of PAT
272 91501 (,50) with the circle areas proportional to vesicle volume. Again, considerable
273 scatter is observed, particularly among the smaller vesicles. However, the larger vesicles
274 define a distinct cluster trending 300° and plunging 40° , with the main outlier attributable
275 to contact with an irregular metal-sulfide mass. This cluster is offset $\sim 33^\circ$ from the
276 orientation defined by the normals to the metal-sulfide contacts.

277 **4.3 Ar-Ar Age**

278 The PAT 91501 Ar-Ar age spectrum (Fig. 5) appears complex but can be
279 interpreted to yield a reliable age. The rate of release of ^{39}Ar and changes in the K/Ca
280 ratio and the Ar-Ar age as a function of extraction temperature all suggest that ^{39}Ar is
281 contained in three distinct diffusion domains— 0-17%, 17-80%, and 80-100% ^{39}Ar release
282 (Fig 5). The ^{39}Ar release data can be modeled by standard diffusion theory in terms of
283 the parameter D/a^2 , where D is the diffusion coefficient and a is the average diffusion
284 length for Ar in the degassing grains. On an Arrhenius plot (argon released vs. $1/T$; not
285 shown), data for these three domains give separate linear trends, each one characterized
286 by a different value of D/a^2 . Above 80% ^{39}Ar release, the observed decreases in age and
287 K/Ca are interpreted to represent release of excess ^{39}Ar recoiled during irradiation into
288 the surfaces of pyroxene grains. Below $\sim 17\%$ ^{39}Ar release, the higher ages are

289 interpreted to represent loss of recoiled ^{39}Ar from surfaces of grains possessing a
290 relatively larger K/Ca ratio. Between ~19% and 80% of the ^{39}Ar release, the K/Ca ratio
291 is relatively constant and the Ar-Ar ages describe a plateau. Ten extractions releasing 19-
292 78% of the ^{39}Ar define an age of 4.463 ± 0.009 Gyr, where the age uncertainty is
293 approximately one-sigma and includes the uncertainty in the irradiation constant, J .
294 Seven extractions releasing 30-78% of the ^{39}Ar give an age of 4.461 ± 0.008 Gyr. To
295 examine these data in an isochron plot, we adopted the cosmogenic ^{38}Ar concentration
296 given below and used the measured $^{37}\text{Ar}/^{36}\text{Ar}$ ratios for each extraction to apportion the
297 measured ^{36}Ar into trapped and cosmogenic components. An isochron plot of $^{40}\text{Ar}/^{36}\text{Ar}$
298 versus $^{39}\text{Ar}/^{36}\text{Ar}$, using trapped ^{36}Ar , is highly linear ($R^2=0.9995$) and its slope yields an
299 age of 4.466 ± 0.0012 Myr, in agreement with the plateau age. The isochron intercept
300 value of $^{40}\text{Ar}/^{36}\text{Ar} = -79 \pm 156$ suggests all ^{40}Ar released in these extractions is radiogenic.
301 The total age summed across all extractions is 4.442 Gyr and suggests that little to no
302 ^{40}Ar was lost from the sample by diffusion over geologic time. We conclude that impact
303 resetting of the K-Ar age occurred 4.46 ± 0.01 Gyr ago.

304 **4.4 Cosmogenic Noble Gases and Radionuclides.**

305 PAT 91501 ,109 (33.4 mg) was heated in two temperature steps and sample ,106
306 (50.0 mg) was heated in four steps (Table 1). In both samples approximately half of the
307 ^3He was released at 500°C . In sample ,106 the peak of the Ne release occurred at 900-
308 1200°C , and the peak of the ^{38}Ar release occurred at 1200°C . Measured ^3He is entirely
309 cosmogenic. The summed $^{20}\text{Ne}/^{22}\text{Ne}$ ratios of 0.845-0.847 indicate that measured Ne is
310 also entirely cosmogenic. Consequently we summed concentrations for each Ne isotope
311 across all extractions to obtain total cosmogenic abundances. Measured $^{36}\text{Ar}/^{38}\text{Ar}$ ratios

312 varied over 0.72-1.75 and indicate the release of trapped Ar, which is mostly adsorbed
313 atmospheric Ar, particularly at lower extraction temperatures. We assumed $^{36}\text{Ar}/^{38}\text{Ar}$
314 ratios of 5.32 for trapped Ar and 0.67 for cosmogenic Ar and calculated the abundances
315 of cosmogenic ^{38}Ar for each extraction. The $^{38}\text{Ar}_{\text{cos}}$ abundances were then summed
316 across each extraction to obtain the total abundance of $^{38}\text{Ar}_{\text{cos}}$. From analyses of He, Ne,
317 and Ar delivered from a standard gas pipette, we estimate the uncertainty in these
318 abundances as $\sim\pm 10\%$.

319 Cosmogenic abundances and $^{22}\text{Ne}/^{21}\text{Ne}$ ratios for the two PAT samples are given
320 in Table 2. Cosmogenic abundances of ^3He , ^{21}Ne , and ^{38}Ar in the two samples agree with
321 each other within their individual uncertainties of $\pm 10\%$. The measured $^{20}\text{Ne}/^{21}\text{Ne}$ ratios
322 for ,109 and ,106 are identical at 0.847 ± 0.005 and 0.845 ± 0.015 . The measured
323 $^{22}\text{Ne}/^{21}\text{Ne}$ ratios of 1.084 ± 0.003 and 1.097 ± 0.003 differ slightly, which probably reflects
324 a shielding difference. A plot of $^3\text{He}/^{21}\text{Ne}$ versus $^{22}\text{Ne}/^{21}\text{Ne}$ defines a shielding trend for
325 many chondrites (Eberhardt et al., 1966). Sample ,109 plots on this shielding trend, but
326 sample ,106 plots slightly above the trend, as a consequence of its lower ^{21}Ne
327 concentration. This observation may imply that in our ,106 sample the concentration of
328 Mg, the main target for $^{21}\text{Ne}_{\text{cos}}$ production, was slightly less than the chondritic value.
329 There is no suggestion of diffusive loss of ^3He in either sample, in spite of the
330 observation that He degassed at relative low temperature in the laboratory (Table 1).

331 The measured abundances of ^{10}Be for three PAT samples agree within their
332 uncertainties (Table 2). The measured activities of ^{26}Al in four PAT samples (Table 2)
333 span a range of $\sim 17\%$.

334 **4.5 PAT Pre-Atmospheric Size**

335 The $^{22}\text{Ne}/^{21}\text{Ne}$ ratio of ~ 1.09 indicates that the pre-atmospheric shielding
336 experienced by PAT 91501 was somewhat greater than that for typical chondrites. The
337 maximum dimension of the recovered meteorite was ~ 19 cm, which, for the purpose of
338 modeling calculations, sets a minimum radius in space of ~ 10 cm. Modeling of the
339 $^{22}\text{Ne}/^{21}\text{Ne}$ ratio in L-chondrites (Leya et al., 2000) predicts that as the meteoroid radius
340 increases, $^{22}\text{Ne}/^{21}\text{Ne}$ ratios as low as ~ 1.09 are first reached in the center of a body with a
341 pre-atmospheric radius of ~ 30 cm. Thus a somewhat larger body presumably carried the
342 physically separate samples that we analyzed. According to the calculations of both Leya
343 et al. (2000) and Masarik et al. (2001), $^{22}\text{Ne}/^{21}\text{Ne}$ ratios plateau at 1.09 ± 0.01 for pre-
344 atmospheric depths from 10 to ≥ 30 cm in L chondrites with radii of 40 cm.

345 The $^{22}\text{Ne}/^{21}\text{Ne}$ ratio is not useful for setting an upper bound on the pre-
346 atmospheric radius. For this purpose we use the ^{26}Al activity. After a cosmic ray
347 exposure lasting more than 20 My (see below) activities of ^{26}Al (and ^{10}Be) would have
348 reached saturation and are therefore equal to average production rates in space –
349 assuming the terrestrial age of PAT was less than 50 kyr or so as suggested by the normal
350 $^{26}\text{Al}/^{10}\text{Be}$ ratios for three samples. According to the calculations of Leya et al. (2000),
351 only meteoroids with radii between 32 cm and 85 cm have the range of ^{26}Al activities
352 observed in PAT. The ^{10}Be activities of PAT 91501 are comparable to those of the L5
353 chondrite St-Robert (Leya et al., 2001), which is thought to have had a pre-atmospheric
354 radius between 40 and 60 cm. We conclude that the pre-atmosphere radius of PAT
355 91501 was in this range.

356 **4.6 Cosmic Ray Exposure Age.**

357 Cosmic Ray Exposure (CRE) ages of stony meteorites were initiated by impacts
358 that reduced meteoroids to objects meter-size or smaller and are almost all <100 Myr for
359 stones (Herzog, 2004). To calculate cosmic ray exposure ages for PAT (Table 2), we
360 used the cosmogenic production rates for L-chondrites given by Eugster (1988), except
361 that the ^{38}Ar production rate was lowered by 11%, as suggested by Graf and Marti
362 (1995). The production rates were corrected for shielding using the measured $^{22}\text{Ne}/^{21}\text{Ne}$
363 ratios. The differences among ages calculated from He, Ne, and Ar for a given sample
364 are greater than the differences in the same age between the two samples. This pattern
365 suggests that most of the apparent variation in CRE age is produced by our choice of
366 production rates. Because cosmogenic Ar is more sensitive to likely compositional
367 variations and because there is some chance that cosmogenic Ar was incompletely
368 extracted, we give greater weight to the ^3He and ^{21}Ne ages and obtain a CRE age for PAT
369 91501 of 25-29 Myr.

370 We also calculated CRE ages based on the ^{26}Al - ^{21}Ne - $^{22}\text{Ne}/^{21}\text{Ne}$ and ^{10}Be - ^{21}Ne -
371 $^{22}\text{Ne}/^{21}\text{Ne}$ equations of Graf et al. (1990a) by using data for the two samples known to
372 have been adjacent to each other ,34 and ,106. The results, 29.6 Myr and 25.5 Myr,
373 respectively, are in the same range as the CRE ages calculated from the noble gases
374 alone. Finally, we calculated the ^{10}Be - ^{21}Ne CRE age for the ,34 -,106 pair by using the
375 formula of Leya et al. (2000) after modifying it for a ^{10}Be half life of 1.5 My. This age,
376 21.9 My, is about 15-26% lower than the others. Leya et al. (2000) observed that their
377 equation for ^{10}Be - ^{21}Ne CRE ages gives a low result for another large L-chondrite,
378 Knyahinya (preatmospheric radius ~45 cm; Graf et al., 1990b). They attribute the

379 discrepancy to their model's underestimation of ^{10}Be production rates in meteoroids the
380 size of Knyahinya and larger.

381

5. DISCUSSION

382 Among ordinary chondrites, the L chondrites record a particularly severe history
383 of impact bombardment, with almost 5% of this group containing shock melts (La Croix
384 and McCoy, 2007). In this regard, PAT 91501 is not atypical. Indeed, its similarity to
385 the impact-melted Shaw L chondrite was noted during its initial description (Marlow et
386 al., 1992). However, the ancient age, vesicular nature, presence of preserved, cm-sized
387 metal-troilite intergrowths, and orientation of both the vesicles and metal-sulfide particles
388 are unusual. These features promise new insights into the timing of and physical
389 processes occurring during the formation of this impact-melted L chondrite.

390 5.1 Chronology

391 Chronological evidence for collisional events on asteroids very early in Solar
392 System history is sparse. Among achondrites, some unbrecciated eucrites may have been
393 excavated from depth on Vesta by a large impact ~ 4.48 Gyr ago (Yamaguchi et al., 2001;
394 Bogard and Garrison, 2003). Within the chondrites, McCoy et al. (1995) reported ages of
395 enstatite chondrite impact melts dating to before 4.3 Gyr and Dixon et al. (2004)
396 suggested that Ar-Ar ages of ~ 4.27 Gyr for a few LL-chondrites may date the time of one
397 or more impact events on the parent body. Taken alone, Ar-Ar ages between ~ 4.38 to
398 ~ 4.52 Gyr can be ambiguous, as ancient ages may reflect either a late impact or slow
399 cooling after parent body metamorphism (Turner et al., 1978; Pellas & Fiéni, 1988). In
400 contrast, impact melts provide a more direct means for dating the timing of collisional
401 events. Most impact melts give Ar-Ar ages less than 1 Gyr, suggesting that melting and

402 re-solidification took place recently, either during events confined to the surfaces of
403 modern asteroids or, perhaps, when collisions on asteroids melted partially and launched
404 meteoroids into Earth-crossing orbits. This population of more recently-formed impact
405 melt rocks includes the vesicular meteorites Cat Mountain (Kring et al., 1996) and Chico
406 (Bogard et al., 1995).

407 In contrast, PAT 91501 dates to the earliest history of the Solar System at 4.461
408 Gyr. Until this work, Shaw was the only ordinary chondrite known to be a near total
409 impact melt (Taylor et al., 1979) and have an Ar-Ar age consistent with an early (>4.0
410 Gyr ago) impact (Turner et al., 1978). Indeed, PAT 91501 shares a number of features
411 with Shaw, particularly its light-colored lithology, petrographic texture and clast-free
412 nature (Taylor et al., 1979). Based on its cosmogenic noble gas concentrations, Shaw has
413 a much younger, nominal one-stage CRE age of ~0.6 My, although in all likelihood,
414 Shaw had a complex exposure history with a first stage that probably lasted >10 Myr
415 (Herzog, 1997). In any event, cosmic-ray exposure ages greater than 1 Gyr are unheard
416 of in stones and thus Shaw's old Ar/Ar age indicates that the meteoroid did not melt (and
417 hence lose an appreciable fraction of its radiogenic ⁴⁰Ar) when it was launched from the
418 asteroid. The 4.46 Gyr impact event that formed PAT 91501 apparently took place
419 considerably earlier than those impacts that reset the Ar-Ar ages of Shaw (4.40 ±0.03 and
420 4.42 ±0.03 Gyr; Turner et al, 1978). We conclude that PAT 91501 and Shaw formed in
421 different impact events on the L-chondrite parent body, and that the two meteorites were
422 not located in close proximity. There seems little question that PAT 91501 is closely
423 related to the bulk of L chondrites and this relationship is supported by the CRE age for
424 PAT of 25-29 Myr, which lies within a diffuse ~22-30 Myr cluster in the distribution of

425 L-chondrite CRE ages. The 4.46 Gyr impact for PAT 91501 falls within the range of Ar-
426 Ar metamorphic ages of relatively unshocked chondrites (Turner et al., 1978; Pellas &
427 Fiéni, 1988). This observation implies that the L parent body experienced a significant
428 impact while it was still relatively warm. In all likelihood, these events occurred on the
429 original L chondrite parent body prior to any subsequent collisions and breakups that
430 would have formed modern asteroids. These early impacts left PAT 91501 deeply buried
431 until it was excavated and launched toward Earth ~28 Myr ago.

432 **5.2 Vesicle Formation**

433 PAT 91501 is remarkable for its mm- to cm-sized vesicles. Vesicles of this size
434 have never before been observed in an impact-melt rock. The few vesicular meteorites
435 that have been investigated in detail are basaltic eucrites or angrites, where vesicles are
436 formed by gases liberated or generated during silicate partial melting (McCoy et al., 2006
437 and references therein). In terrestrial systems, H₂O is the typical vesicle-forming gas, as
438 it is abundant in the Earth's crust and exsolves from basaltic magmas at relatively
439 shallow depths (Oppenheimer, 2004). In contrast, chemical analyses (Jarosewich, 1990)
440 and the presence of abundant Fe,Ni metal suggest that ordinary chondrites likely were
441 very dry systems and, thus, H₂O is unlikely as a major vesicle-forming gas. McCoy et al.
442 (2006) argued that a mixed CO-CO₂ gas was responsible for vesicle formation in
443 asteroidal basalts and the contribution of such a gas cannot be unequivocally eliminated.
444 The contribution of volatiles from the impactor, such as ice in a cometary body, or
445 volatilization of silicates at superheated temperatures also seems unlikely, although
446 impossible to rule out.

447 A much more likely source of volatiles is sulfur vaporization during impact
 448 melting. Numerous previous studies have pointed to the role of sulfur vaporization
 449 during metamorphic and impact processes of ordinary chondrites. Lauretta et al. (1997)
 450 showed that a small amount of sulfur vaporizes at the metamorphic temperatures of
 451 ordinary chondrites. Sulfur vaporization is also a common problem in ordinary chondrite
 452 melting experiments (e.g., Jurewicz et al., 1995) and has been invoked to explain the
 453 formation of sulfide-rich regions in the Smyer H chondrite impact melt breccia (Rubin,
 454 2002). In PAT 91501, the larger vesicles have metal-sulfide intergrowths associated with
 455 them, suggestive of formation by sulfide vaporization during impact melting

456 We can calculate the amount of S gas required to create the abundance of vesicles
 457 (~2 vol.%) documented with computer tomography. The formula for the bulk density β
 458 of a vesicular material is

$$459 \quad 1/\beta = n / \rho_g + (1 - n) / \rho_{ng} \quad (1)$$

460 where ρ_g is the gas density, ρ_{ng} is the density of the non-gas part (i.e. solid or liquid) and
 461 n is the mass fraction of gas. If the conditions are such that the gas law holds at least
 462 approximately, the density of the gas is given by

$$463 \quad \rho_g = (m P) / (Q T) \quad (2)$$

464 where m is the molecular weight of the gas, P is its pressure, Q is the universal gas
 465 constant (8314 J/kmol) and T is the gas temperature. Substituting for ρ_g :

$$466 \quad 1/\beta = (n Q T)/(m P) + (1 - n) / \rho_{ng} \quad (3)$$

467 The two terms on the right are the partial volumes of gas and non-gas, respectively, so the
 468 gas volume fraction v_g is given by

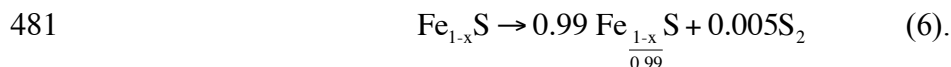
$$469 \quad v_g = [(n Q T)/(m P)] / [(n Q T)/(m P) + (1 - n) / \rho_{ng}] \quad (4)$$

470 which is more conveniently re-arranged as

471
$$n / (1 - n) = (v_g m P) / [(1 - v_g) \rho_{ng} Q T] \quad (5)$$

472 Using the values we estimated, $v_g = 0.02$, $T = 1670$ K, $\rho_{ng} = 3520$ kg m⁻³, $m = 64$ for S₂ or
473 SO₂, and $P = 5 \times 10^5$ Pa for a depth of a few km in a 50 km radius asteroid, appropriate to
474 the lithostatic load likely to occur in a silicate melt at depth, we find $[n / (1 - n)] = 1.448 \times$
475 10^{-5} , so that $n = 1.448 \times 10^{-5}$ to the same precision. If we regard this as the abundance of
476 S₂, it indicates that ~15 ppm of gas are necessary for formation of the vesicles, in
477 excellent agreement with earlier calculations of S₂ generated in equilibrium with sulfide
478 in PAT 91501.

479 Alternatively, we can estimate the amount of S₂ gas produced by vaporization if
480 all the FeS in a chondrite melted using the following equation from Lauretta et al. (1997):



482 Thus, each mole of sulfide liberates 0.005 moles of S₂. So for a typical L-
483 chondrite mode of FeS (~4.2vol%), it would be expected that ~210 ppm of S₂ would form
484 during melting. While this may seem like a small amount, the vesicle volume produced
485 by this amount of gas would be much greater than that observed in PAT 91501. As we
486 discuss in the next section, the amount of sulfide present in the impact melt likely results
487 from gravitational segregation of the dense metal-sulfide particles in the silicate melt. It
488 is likely that the amount of sulfide that actually vaporized is much closer to about one-
489 tenth that of average L chondrites, thus, a S₂ gas abundance of ~20 ppm is probably more
490 reasonable.

491 The abundance of 15-20 ppm S₂ required for vesicle formation and in equilibrium
492 with sulfide is a vanishingly small amount, as also noted for the abundance of CO-CO₂ in

493 vesicular angrites and eucrites by McCoy et al. (2006). Thus, it is no surprise that
494 evidence for its condensation cannot be found. No sulfide or sulfur linings have been
495 observed on vesicle walls in PAT 91501, although moderate terrestrial weathering has
496 occurred in the meteorite and hydrated iron oxides of terrestrial origin commonly occur
497 as vesicle linings. We considered the possibility that pentlandite found in the metal-
498 sulfide assemblages might reflect S volatilization. However, no isotopic fractionation
499 consistent with S volatilization was observed between pentlandite and troilite and, as
500 discussed later, it appears more likely that pentlandite is an equilibrium phase formed
501 during cooling in the Fe-Ni-S system.

502 **5.3 Physical Setting and formation of PAT 91501**

503 While PAT 91501 joins a growing list of impact-melted rocks from the L
504 chondrite parent body, its ancient age and large metal-sulfide nodules and vesicles and
505 their striking orientation are unique. Whereas it lacks the abundant clasts observed in
506 many impact melt breccias, similar clast-poor lithologies are observed in Shaw and, most
507 notably, as a 30 cm wide vein in Chico (Bogard et al., 1995).

508 Mittlefehldt and Lindstrom (2001) suggested that PAT 91501, because of its
509 homogeneously melted nature and relatively slow cooling compared to other impact melts,
510 could be part of an impact melt basal layer found on the floor of a crater (Melosh, 1989)
511 or as a melt dike injected into surrounding country rock (Stöffler et al., 1991). Our work
512 provides additional constraints to distinguish between these two settings. There are
513 several reasons to question the formation of PAT 91501 in a crater floor melt sheet. On
514 Earth, these melt sheets tend to experience rapid cooling and be clast laden. Only in the
515 very largest terrestrial craters (e.g., Manicouagan, Sudbury) where impact melt sheets

516 exceed 200 m in thickness are clast-poor, igneous textured rocks observed (Keil et al.,
517 1997). Likewise, fragmentation of a vesicular lava flow or impact melt sheet will occur
518 at the surface of a low-gravity, atmosphereless body. To achieve the equivalent of
519 terrestrial atmospheric pressure, McCoy et al. (2006) calculated that a melt sheet ~130 m
520 thick would be needed on a body ~250 km in radius. These two estimates are in good
521 agreement and suggest the need for a melt sheet in excess of 100 m thickness. An impact
522 event capable of producing such a thick melt sheet on an asteroid would, instead,
523 collisionally disrupt the body (Keil et al., 1997). Thus, we suggest that a melt dike
524 injected into the surrounding country rock below the impact crater is a more viable
525 setting for the formation of PAT 91501.

526 Injection of molten chondritic material into the surrounding country rock provides
527 both moderate pressure necessary for vesicle retention and a thermal environment
528 conducive to rapid cooling without quenching. We have been unable to constrain the
529 cooling rate. Although zoning within the large taenite particles might normally be taken
530 as indicative of cooling, we argue instead that the assemblage taenite (γ)-troilite-
531 pentlandite is an equilibrium assemblage formed during cooling at temperatures between
532 ~300-500 °C, consistent with phase relations in the Fe-rich portion of the Fe-Ni-S system
533 (Ma et al., 1998). With the surrounding country rock cooler than the melt, solidification
534 could have occurred in a matter of hours. The absence of distinct clasts in PAT 91501 is
535 not inconsistent with such a model. While most impact melt breccias, by definition,
536 contain clastic material from the country rock, subcrater melt dikes on Earth exhibit a
537 range of widths (Keil et al., 1997) and it is reasonable to assume that PAT 91501 sampled
538 one of the wider, clast-free portions of a dike. Indeed, Bogard et al. (1995) argue that a

539 30 cm wide zone of clast-poor impact melt in Chico samples such an intrusive dike. At a
540 maximum dimension of ~20 cm, PAT 91501 would not be extraordinary in this regard.

541 Although cooling and crystallization may have occurred relatively rapidly in this
542 dike, we suggest that it was far from a quiescent environment. Despite the preservation
543 of metal and sulfide as mm- to cm-sized nodules, it is clear from the bulk elemental
544 composition that metal and sulfide were lost from the system. Comparison of metal and
545 sulfide abundances in PAT 91501 (~0.3 and ~0.5 vol.%, respectively) with those reported
546 for average L chondrites (3.7 and 4.2 vol.%, respectively; McSween et al., 1991) suggests
547 that the melt from which PAT 91501 crystallized lost ~90% of the metal and sulfide
548 component prior to solidification. This loss is not surprising, given the marked density
549 contrast between molten metal, sulfide and silicate. In fact, a similar density contrast
550 exists between molten silicates and the vesicles, leading to rapid rise within the melt. The
551 velocity, u , of settling or rising is determined using the Stoke's velocity equation
552 (Turcotte and Schubert, 2002)

553
$$u = \frac{1}{3} \frac{\Delta\rho r^2 g}{\eta} \quad (7)$$

554 where $\Delta\rho$ is the difference in density between the metal, sulfide or vesicles and the
555 silicate melt; r is the radius of the grain of metal or sulfide or vesicle; g is gravity for an
556 assumed 50 km radius parent body (0.012 m/s²); and η is the viscosity of the silicate melt
557 through which the metal, sulfide or vesicle is moving. We estimated the liquidus
558 temperature of bulk L-chondrite composition to be between 1400 and 1600 °C, which
559 affects the viscosity of the melt. Using the maximum size of the metal, sulfide and
560 vesicles determined from the CT scan, we calculate that the largest vesicle would rise at
561 ~3 m/hr while the largest metal particle would sink at ~2 m/hour.

562 One of the most astonishing results from the CT scans is the orientation of the
563 metal/sulfide intergrowths. These orientations, reflected in the relative orientation of
564 metal to sulfide (Fig. 3) and the orientations of metal-sulfide contacts and vesicle
565 elongation – are consistent with formation in a gravitational field. In this respect, PAT
566 91501 is exceptional in that we know which way was up while on the asteroid. This
567 orientation is illustrated in Fig. 3. To the best of our knowledge, only one other meteorite
568 can claim such a distinction. In the Cape York meteorite (Kracher et al., 1977; Buchwald,
569 1987), elongate troilite inclusions contain chromites concentrated at one end and
570 phosphates at the other, which may be indicative of formation in a gravitational field
571 (Kracher and Kurat, 1975), but have also been attributed to melt migration in a thermal
572 gradient (Buchwald, 1987).

573 In practice, calculated velocities probably represent theoretical maximums, as the
574 vesicles likely coalesced during rise while the metal particles typically contain significant
575 amounts of attached, less-dense sulfide. Nonetheless, these calculations suggest that
576 metal-sulfide particles and vesicles should have rapidly segregated from the volume of
577 melt that eventually crystallized to form PAT 91501.

578 Unless this rock happened to capture a snapshot of metal-sulfide particles sinking
579 and vesicles rising, the retention of any vesicles or metal-sulfide requires another
580 explanation. Far from being dominated by gravitational settling or rising under the
581 influence of buoyancy alone, we suggest that the system was also influenced by the
582 movement of melt within the fracture and the binding of dense metal-sulfide and buoyant
583 vesicles to produce particles of near-neutral buoyancy. When the melt was injected into
584 the cold country rock, it began to rise due to the marked thermal difference between the

585 melt and country rock. Using the method of Wilson and Head (1981), we calculate that
586 the melt rose at a velocity of 0.028 m/s through the dike and solidified due to cooling
587 after migration of ~220 m (McCoy et al., 2006). At this rate, the magma solidified after
588 rising through the dike for ~2 hours. Importantly, the rate of rise of the melt through the
589 dike was roughly an order of magnitude faster than the rate of metal-sulfide settling or
590 vesicle rise. Thus, settling of metal and sulfide to the bottom of the dike was inhibited by
591 the rapid rise of melt through the dike.

592 It also bears noting that the gravitational vector inferred from the metal-sulfide
593 contacts is inconsistent with the orientation of the vesicle long axes (Fig. 4). This slight
594 offset may result from minor turbulence in the rising magma, or possibly an additional
595 lateral component of melt movement that would be reflected in the vesicle shapes but not
596 the gravitational settling of the metal.

597 Finally, the preservation of metal-sulfide-vesicle assemblages may result from the
598 offsetting differences in density and buoyancy. It is interesting to note that the upward
599 velocities of the average-sized gas bubbles responsible for the vesicles and the downward
600 velocity of the average-sized metal-sulfide grains are very similar at all temperatures. If
601 surface tension forces bind bubbles and grains of comparable size together, offsetting
602 buoyancy may be created that would cause the linked bubbles and sulfide grains to be
603 suspended, or at least to move only very slowly, in the melt. Neutral buoyancy has been
604 suggested for magnetite and vesicles in the Bishop Tuff, where a vesicle either scavenged
605 magnetite crystals from the melt or served as a nucleation point for magnetite growth, in
606 the pre-eruptive magma (Gualda and Anderson, 2007). The attainment of neutral

607 buoyancy in the upward moving melt from which PAT 91501 crystallized might explain
608 the retention of even large metal-sulfide particles.

609

6. CONCLUSIONS

610 Among the abundant impact melt rocks and breccias from the L chondrite parent
611 body, PAT 91501 is unique in exhibiting cm-sized metal-sulfide particles and vesicles,
612 for the remarkable alignment of these particles, and for its ancient age. Sulfur
613 volatilization must have been a ubiquitous process during impact melting of chondritic
614 materials and other meteorites (e.g., Chico) are known that reasonably sample impact
615 melt dikes injected into the crater basement. These other meteorites do not exhibit the
616 large vesicles seen in PAT 91501. This sample must have formed by a combination of a
617 particularly large, early impact on the L chondrite parent body that formed unusually
618 wide, clast free melt veins where the combination of relatively slow cooling and
619 crystallization, coalescence and rise of vesicles, coalescence and sinking of metal-sulfide
620 particles, formation of metal-sulfide-vesicle aggregates creating neutrally buoyant
621 assemblages, and upward flow of magma in the dike. Although similar processes must
622 have occurred in the formation of other chondritic impact melt rocks, they did not
623 combine in the unique combination that formed PAT 91501.

624 *Acknowledgements* – We thank Robbie Score, Cecilia Satterwhite, the Meteorite
625 Processing Laboratory at Johnson Space Center, and the Meteorite Working Group for
626 providing samples. Tim Gooding (Smithsonian) provided expert technical assistance.
627 Larry Nittler and Jianhua Wang provided invaluable assistance with ion microprobe
628 analyses of sulfides and the insights of Joe Goldstein and Jijin Yang helped us understand
629 the formation of zoning within the metal-sulfide particles. We thank Bill Carlson for his
630 early collaboration on the computed tomography aspects of this project and Ralph Harvey
631 and Roy Clarke for their insights into the terrestrial and asteroidal history of PAT
632 91501/91516/91528. Aspects of this work were supported by the NASA
633 Cosmochemistry Program (DDB, TJM, GFH) and the Becker Endowment to the
634 Smithsonian Institution (TJM). Facility support and software development at the
635 University of Texas High-Resolution X-ray CT Facility were provided by NSF grants

636 EAR-0345710 and EAR-0113480.
637

REFERENCES

- 637
638
639 Bogard D.D. (1995) Impact ages of meteorites: A synthesis. *Meteoritics* **30**, 244-268.
640 Bogard D.D. and Hirsch W.C. (1980) $^{40}\text{Ar}/^{39}\text{Ar}$ dating, Ar diffusion properties, and
641 cooling rate determinations of severely shocked chondrites. *Geochim. Cosmochim.*
642 *Acta* **44**, 1667-1682.
643 Bogard D.D. and Garrison D.H. (2003) ^{39}Ar - ^{40}Ar ages of eucrites and thermal history of
644 asteroid 4 Vesta. *Meteoritics & Planetary Science*, **38**, 669-710
645 Bogard D.D., Garrison D.H., Norman M., Scott E.R.D., and Keil K. (1995) ^{39}Ar - ^{40}Ar age
646 and petrology of Chico: Large-scale impact melting on the L chondrite parent body.
647 *Geochim. Cosmochim. Acta* **59**, 1383-1399.
648 Buchwald V.F. (1987) Thermal migration III: Its occurrence in Cape York and other iron
649 meteorites. *Meteoritics* **22**, 343-344.
650 Clarke R.S. Jr. (1994) In *Ant. Meteorite News*. (Score R. and Lindstrom M.M., Eds.) *Ant.*
651 *Meteorite News*. **17**, #1, 15-16. NASA Johnson Space Center, Houston, Texas,
652 USA.
653 Dixon, E. T.; Bogard, D. D.; Garrison, D. H.; Rubin, A. E. (2004) ^{39}Ar - ^{40}Ar evidence for
654 early impact events on the LL parent body. *Geochim. Cosmochim. Acta*, **68**, 3779-
655 3790.
656 Eberhardt P., Eugster O., Geiss J., and Marti K. (1966) Rare gas measurements in 30
657 stone meteorites. *Naturforsch.* **21A**, 414-426.
658 Eugster O. (1988) Cosmic-ray production rates for He-3, Ne-21, Ar-38, Kr-83, and Xe-
659 126 in chondrites based on Kr-81/Kr exposure ages. *Geochim. Cosmochim. Acta*
660 **52**, 1649-1662.
661 Graf Th. and Marti K. (1995) Collisional records in LL chondrites. *J. Geophys. Res.*
662 *(Planets)* **100**, 21247-21263.
663 Graf Th., Signer P., Wieler R., Herpers U., Sarafin R., Vogt S., Fieni Ch., Pellas P.,
664 Bonani G., Suter M., and Wölfli W. (1990a) Cosmogenic nuclides and nuclear
665 tracks in the chondrite Knyahinya. *Geochim. Cosmochim. Acta* **54**, 2511-2520.
666 Graf Th., Baur H., and Signer P. (1990b) A model for the production of cosmogenic
667 nuclides in chondrites. *Geochim. Cosmochim. Acta* **54**, 2521-2534.
668 Gualda G.A.R. and Anderson A.T. Jr. (2007) Magnetite scavenging and the buoyancy of
669 bubbles in magma. Part 1: Discovery of a pre-eruptive bubble in Bishop rhyolite.
670 *Contrib. Mineral. Petrol.* **153**, 733-742.
671 Haack, H., Farinella, P., Scott E.R.D., and Keil, K (1996) Meteoritic, asteroidal, and
672 theoretical constraints on the 500 MA disruption of the L chondrite parent body.
673 *Icarus* **119**, 182-191.
674 Hartmann W.K., Ryder G., Dones L., and Grinspoon D. (2000) The time-dependent
675 intense bombardment of the primordial Earth/Moon system. In *Origin of the Earth*
676 *and Moon* (R.M. Canup and K. Righter, eds.), University of Arizona Press, Tucson,
677 pp 493-512.
678 Harvey R.P. and Roedder E. (1994) Melt inclusions in PAT 91501: Evidence from
679 crystallization from an L chondrite impact melt. *Lunar Planet. Sci.* **25**, 513.
680 Herzog G.F. (2005) Cosmic-ray exposure ages of meteorites, pp. 347-380. In *Meteorites,*
681 *Comets, and Planets* (ed. A.M. Davis) Vol. 1 *Treatise on Geochemistry* (eds. H.D.
682 Holland and K.K. Turekian), Elsevier-Pergamon, Oxford.

683 Herzog G. F., Vogt S., Albrecht A., Xue S., Fink D., Klein J., Middleton R.,
684 Weber H. W., and Schultz L. (1997) Complex exposure histories for meteorites
685 with "short" exposure ages. *Meteoritics*, **32**, 413-422

686 Jarosewich, E. (1990) Chemical analyses of meteorites: A compilation of stony and iron
687 meteorite analyses. *Meteoritics* **25**, 323-337.

688 Jurewicz A.J.G., Mittlefehldt D.W., and Jones J.H. (1995) Experimental partial melting
689 of the St. Severin (LL) and Lost City (H) chondrites. *Geochim. Cosmochim. Acta*
690 **59**, 391-408.

691 Keil K., Stöffler D., Love S.G., and Scott E.R.D. (1997) Constraints on the role of impact
692 heating and melting in asteroids. *Meteoritics and Planet. Sci.* **32**, 349-363.

693 Ketcham R. A. (2005) Computational methods for quantitative analysis of three-
694 dimensional features in geological specimens. *Geosphere* **1**(1), 32-41.

695 Ketcham R. A. and Carlson W. D. (2001) Acquisition, optimization and interpretation of
696 X-ray computed tomographic imagery: Applications to the geosciences. *Computers*
697 *and Geosciences* **27**, 381-400.

698 Kracher A. and Kurat G. (1975) An unusual phosphate-sulfide assemblage in the Cape
699 York iron meteorite. *Meteoritics* **10**, 429.

700 Kracher A., Kurat G., and Buchwald V.F. (1977) Cape York: The extraordinary
701 mineralogy of an ordinary iron meteorite and its implication for the genesis of
702 IIIAB irons. *Geochem. J.* **11**, 207-217.

703 Kring D.A., Swindle T.D., Britt D.T., and Grier J.A. (1996) Cat Mountain: A meteoritic
704 sample of an impact-melted asteroid regolith. *J. Geophys. Res.*, **101**, 29,353-29,371.

705 La Croix L.M. and McCoy T.J. (2007) Shock Classification of Antarctic Ordinary
706 Chondrites. *Lunar and Planet. Sci. Conf.* **XXXVIII**, abst# 1601.

707 Laretta D.S., Lodders K., Fegley B., and Kremser D.T. (1997) The origin of sulfide-
708 rimmed metal grains in ordinary chondrites. *Earth and Planet. Sci.* **151**, 289-301.

709 Leya I., Lange H.-J., Neumann S., Wieler R., and Michel R. (2000) The production of
710 cosmogenic nuclides in stony meteoroids by galactic cosmic ray particles. *Meteorit.*
711 *Planet. Sci.* **35**, 259-286.

712 Leya I., Wieler R., Aggrey K., Herzog G. F., Schnabel C., Metzler K., Hildebrand A. R.,
713 Bouchard M., Jull A. J. T., Andrews H. R., Wang M.-S., Ferko T. E., Lipschutz M.
714 E., Wacker J. F., Neumann S., and Michel R. (2001) Exposure history of the St-
715 Robert (H5) fall. *Meteorit. Planet. Sci.* **36**, 1479-1494.

716 Ma L., Williams D.B. and Goldstein J.I. (1998) Determination of the Fe-rich portion of
717 the Fe-Ni-S phase diagram. *J. Phase Equilibria* **19**, 299-309.

718 Masarik J., Nishiizumi K., and Reedy R. C. (2001) Production rates of ³He, ²¹Ne and
719 ²²Ne in ordinary chondrites and the lunar surface. *Meteorit. Planet. Sci.* **36**, 643-
720 650.

721 Marlow R., Score R. and Mason B. (1992) In *Ant. Meteorite News*. (Score R. and
722 Lindstrom M.M., Eds.) **15**, #2, 30. NASA Johnson Space Center, Houston, Texas,
723 USA 39pp.

724 McCoy T.J., Keil K., Bogard D.D., Garrison D.H., Casanova I., Lindstrom M.M.,
725 Brearley A.J., Kehm K., Nichols R.H. Jr. and Hohenberg C.M. (1995) Origin and
726 history of impact-melt rocks of enstatite chondrite parentage. *Geochim.*
727 *Cosmochim. Acta* **52**, 161-175.

728 McCoy T.J., Ketcham R.A., Wilson L., Benedix G.K., Wadhwa M., and Davis A.M.
729 (2006) Formation of vesicles in asteroidal basaltic meteorites. *Earth and Planet.*
730 *Sci.* 246, 102-108.

731 McSween H.Y., Bennett M.E., and Jarosewich E. (1991) The mineralogy of ordinary
732 chondrites and implications for asteroid spectrophotometry. *Icarus* **91**, 107-116.

733 Melosh H.J. (1989) *Impact Cratering: A Geologic Process*. Oxford Univ. Press, New
734 York, New York, USA. 245pp.

735 Mittlefehldt D.W and Lindstrom M.M. (2001) Petrology and geochemistry of Patuxent
736 Range 91501 and Lewis Cliff 88663. *Meteoritics and Planet. Sci.* **36**, 439-457.

737 Middleton R. and Klein J. (1986) A new method for measuring $^{10}\text{Be}/^{9}\text{Be}$ ratios. *Proc.*
738 *Workshop Tech. Accel. Mass Spectrom.*, (Eds. R.E.M. Hedges and E.T. Hall) June
739 30-July 1, 1986, Oxford, England, 76-81.

740 Middleton R., Klein J., Raisbeck G.M. and Yiou F. (1983) Accelerator mass spectrometry
741 with aluminum-26. *Nucl. Instru. Meth. Phys. Res.* **218**, 430-438.

742 Oppenheimer C. (2004) Volcanic degassing, in: R. Rudnick (Ed.), *The Crust*, Elsevier-
743 Pergamon, Oxford, pp. 123-166.

744 Pellas P. and Fiéni C. (1988) Thermal histories of ordinary chondrite parent asteroids.
745 *Lunar and Planet. Sci. Conf.* **XIX**, 915-916 (abs).

746 Rubin A.E. (1985) Impact melt products of chondritic material *Rev. Geophys.* 23, 277-
747 300

748 Rubin A.E. (2002) Smyer H-chondrite impact-melt breccia and evidence for sulfur
749 vaporization. *Geochim. Cosmochim. Acta*, **66**, 699-711.

750 Stöffler D., Keil K., and Scott E.R.D. (1991) Shock metamorphism of ordinary
751 chondrites. *Geochim. Cosmochim. Acta* **55**, 3845-3867.

752 Taylor G.J., Keil K., Berkley J.L., Lange D.E., Fodor R.V., and Fruland R.M. (1979) The
753 Shaw meteorites: History of a chondrite consisting of impact-melted and
754 metamorphosed lithologies. *Geochim. Cosmochim. Acta.* **43**, 323-337.

755 Turcotte D. L. and Schubert G. (2002) *Geodynamics* 2nd Ed. Cambridge Univ. Press,
756 New York, New York, USA 456pp.

757 Turner G., Enright M.C., Cadogan P.H. (1978) The early history of chondrite parent
758 bodies inferred from Ar-40-Ar-39 ages. *Proc. 9th Lunar and Planet. Sci. Conf.*,
759 989-1025.

760 Vogt S. and Herpers U. (1988) Radiochemical separation techniques for the
761 determination of long-lived radionuclides in meteorites by means of accelerator
762 mass spectrometry. *Fresenius Z. Anal. Chemie* **331**, 186-188.

763 Wilson L. and Head J.W. (1981) Ascent and eruption of basaltic magma on the Earth and
764 Moon. *J. Geophys. Res.* **86**, 2971-3001.

765 Yamaguchi A., Taylor G. J., Keil K. Floss C., Crozaz G., Nyquist L. E., Bogard D. D.,
766 Garrison D. H., Reese Y. D., Wiesmann H., and Shih C.-Y. (2001) Post-
767 crystallization reheating and partial melting of eucrite EET90020 by impact into the
768 hot crust of asteroid 4Vesta ~4.50 Gyr ago. *Geochim. Cosmochim. Acta*, **65**, 3577-
769 3599.

770

770
771

Table 1. Noble gas abundances in two samples of PAT 91501

	³ He 10 ⁻⁷	⁴ He 10 ⁻⁶	²⁰ Ne 10 ⁻⁸	²¹ Ne 10 ⁻⁸	²² Ne 10 ⁻⁸	³⁶ Ar 10 ⁻⁹	³⁸ Ar 10 ⁻⁹	⁴⁰ Ar 10 ⁻⁵
Sample ,109								
500°C	2.33	8.58	0.32	0.30	0.38	0.53	0.47	1.02
1550°C	2.21	36.60	9.12	9.97	10.76	9.42	10.06	2.62
Sample ,106								
500°C	2.70	5.73	0.31	0.029	0.38	0.48	0.48	1.07
900°C	1.68	24.46	3.30	3.56	3.88	1.53	0.87	1.29
1200°C	0.24	0.34	3.24	3.51	3.83	4.50	5.36	0.62
1550°C	0.03	0.12	1.15	1.26	1.37	1.68	2.35	0.17

772

Table 2. Abundances of cosmogenic species and cosmic-ray exposure ages of PAT 91501.

Sample	,106	,109		
³ He	46.5	45.4		
²¹ Ne	8.62	10.27		
³⁸ Ar	0.86	0.99		
²⁰ Ne/ ²² Ne	0.845±0.015	0.847±0.005		
²² Ne/ ²¹ Ne	1.097±0.003	1.084±0.003		
T ₃	28.7	28.0		
T ₂₁	24.6	27.5		
T ₃₈	20.6	23.1		
T ₁₀₋₂₁	29.6			
T ₂₆₋₂₁	25.5			
Sample	,34	,38	,40	,42
¹⁰ Be	20.8	20.6		20.3
²⁶ Al	64.9	61.9	60.6	55.2

Noble gas concentrations in 10⁻⁸ cm³ STP/g. Cosmic-ray exposure ages, T, in Myr. ¹⁰Be and ²⁶Al activities in dpm/kg; uncertainties are estimated to be ±7%. T₁₀₋₂₁ and T₂₆₋₂₁ after Graf et al. (1990a).

773
774

774

Figure Captions

775 Figure 1. Photograph of PAT 91501 ,50. Numerous vesicles and metal-sulfide grains
776 (up to cm-sized) are visible on the cut surface. Cracks throughout sample are likely
777 due to terrestrial weathering. Scale cube is 1cm on a side.

778 Figure 2. A) Reflected light optical photomicrograph of an intergrown metal-sulfide
779 particle in contact with a vesicle in PAT 91501 (,111). The particle has been etched
780 to show the metallographic texture consisting of mainly taenite (t) and martensite
781 (m). Troilite (tr) with small particles of embedded pentlandite (p) rims the entire
782 particle. B) Nickel composition (following traverse illustrated in A) across the two
783 domains showing high-Ni inclusion-free (or poor) taenite rims grading into
784 intermediate-Ni martensitic cores.

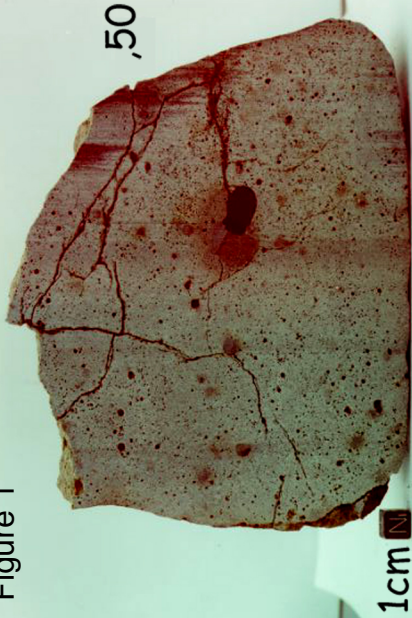
785 Figure 3. A single frame from the 3 dimensional rotation visualization made from the CT
786 scan of PAT 91501 (,50), in which vesicles and metal-sulfide intergrowths are
787 highlighted. Metal (yellow), sulfide (magenta) and vesicles (blue bubbles) are set
788 in a semi-transparent outline of the specimen pictured in Figure 1. Arrow points to
789 prominent, large vesicle seen in Fig. 1. The specimen is oriented as it would have
790 been at the time of crystallization as suggested by the metal-sulfide orientations
791 (sulfide above metal in all instances). Note, however, that long axes of vesicles and
792 metal-sulfide masses are offset somewhat to the left.

793 Figure 4. Stereo plots from PAT 91501 (,50) of a) the normals to the planes defined by
794 the contact between metal and sulfide with the size of the each circle proportional
795 to the area of the contact and b) orientations of the vesicle long axes with the circle
796 areas proportional to vesicle volume. Clustering of orientations are observed for

797 both metal-sulfide contacts and vesicle elongation. See text for discussion of
798 orientation directions.

799 Figure 5. Ar-Ar ages (Gyr, rectangles, left scale) and K/Ca ratios (stepped line, right
800 scale) as a function of cumulative release of ^{39}Ar for temperature extractions of a
801 melt sample of PAT 91501. Seven extractions releasing 30-78% of the ^{39}Ar give an
802 age of 4.461 ± 0.008 Gyr, which we interpret to be the formation time of the PAT
803 91501.

Figure 1



1cm

PAT91501

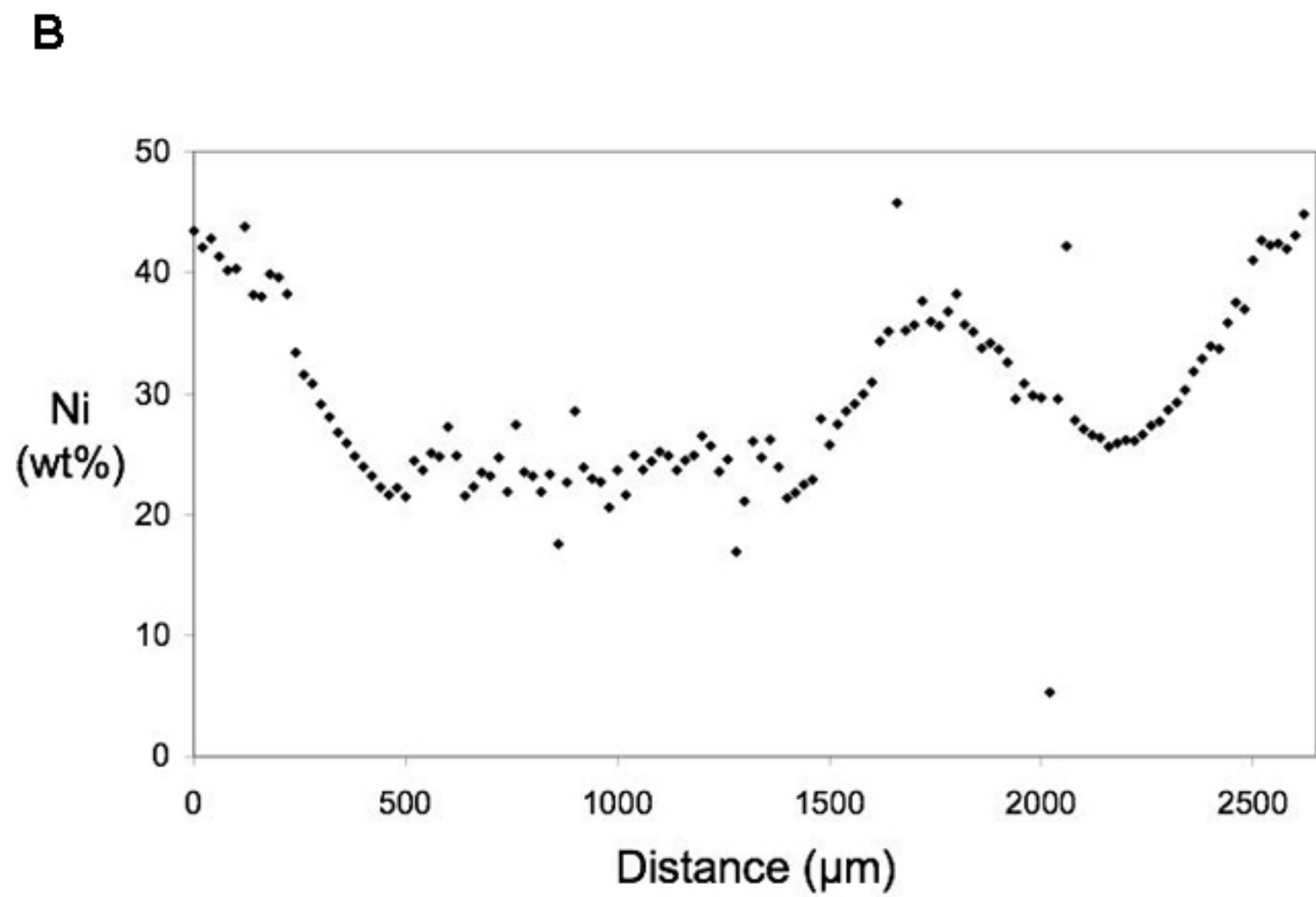
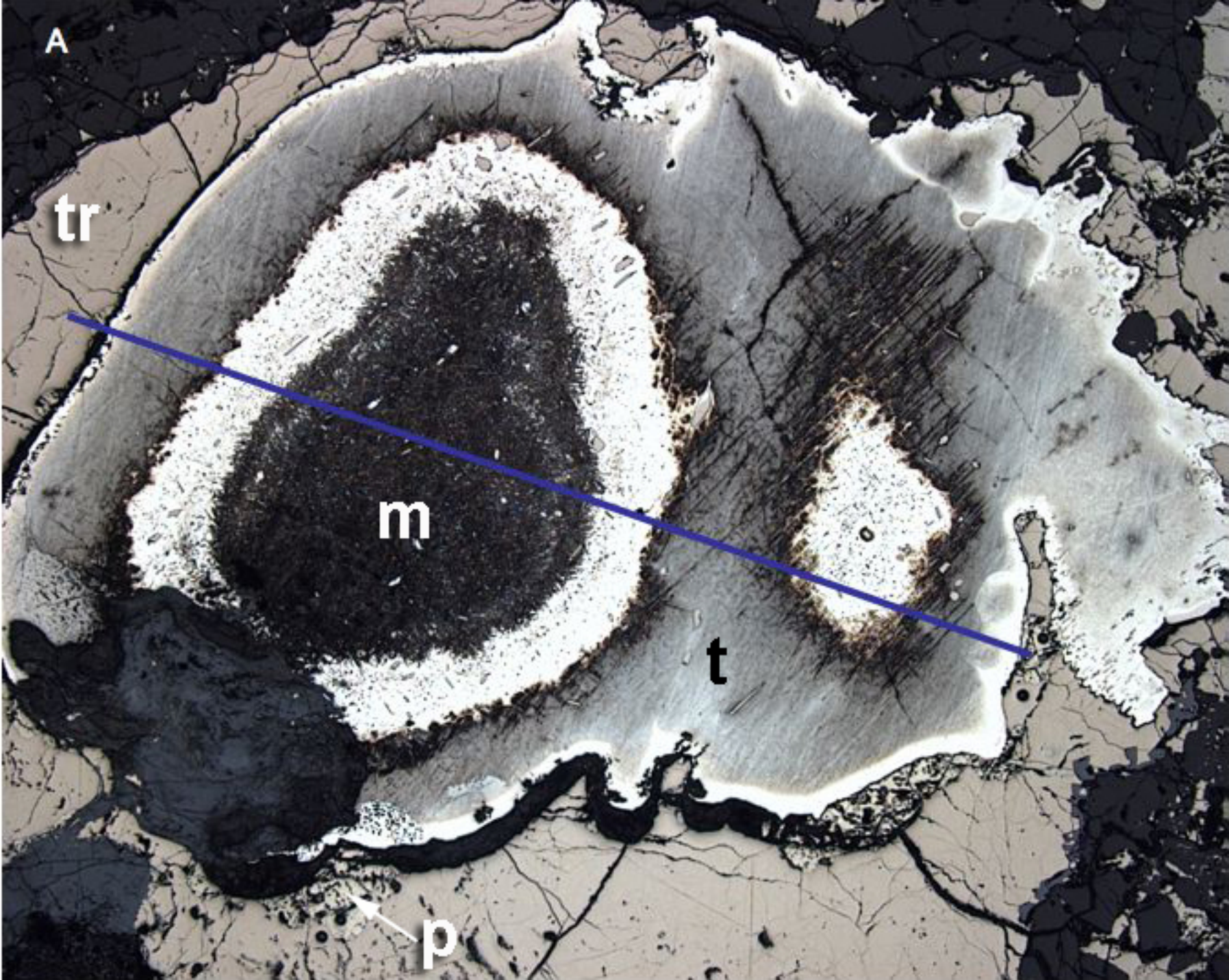


Figure 2

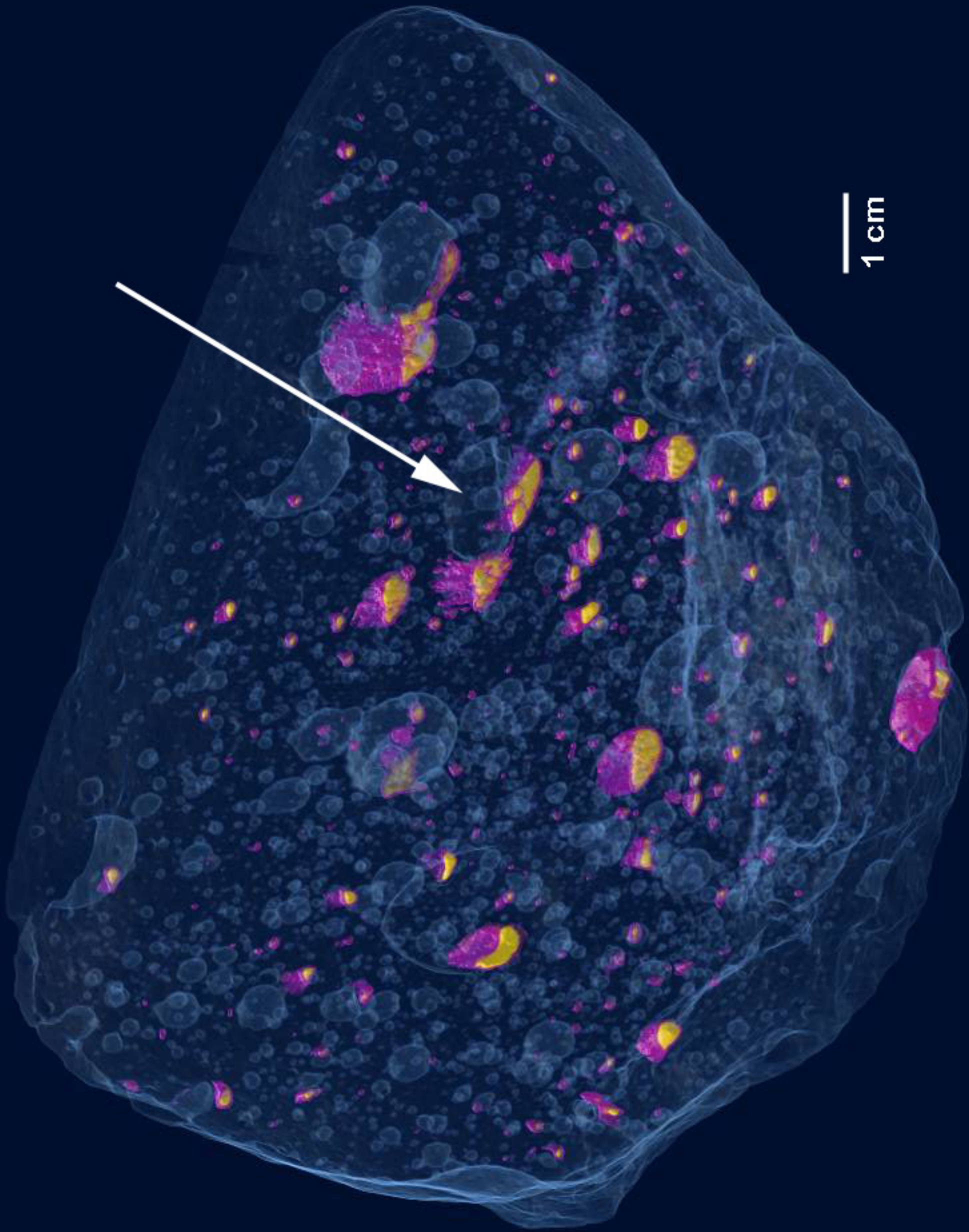
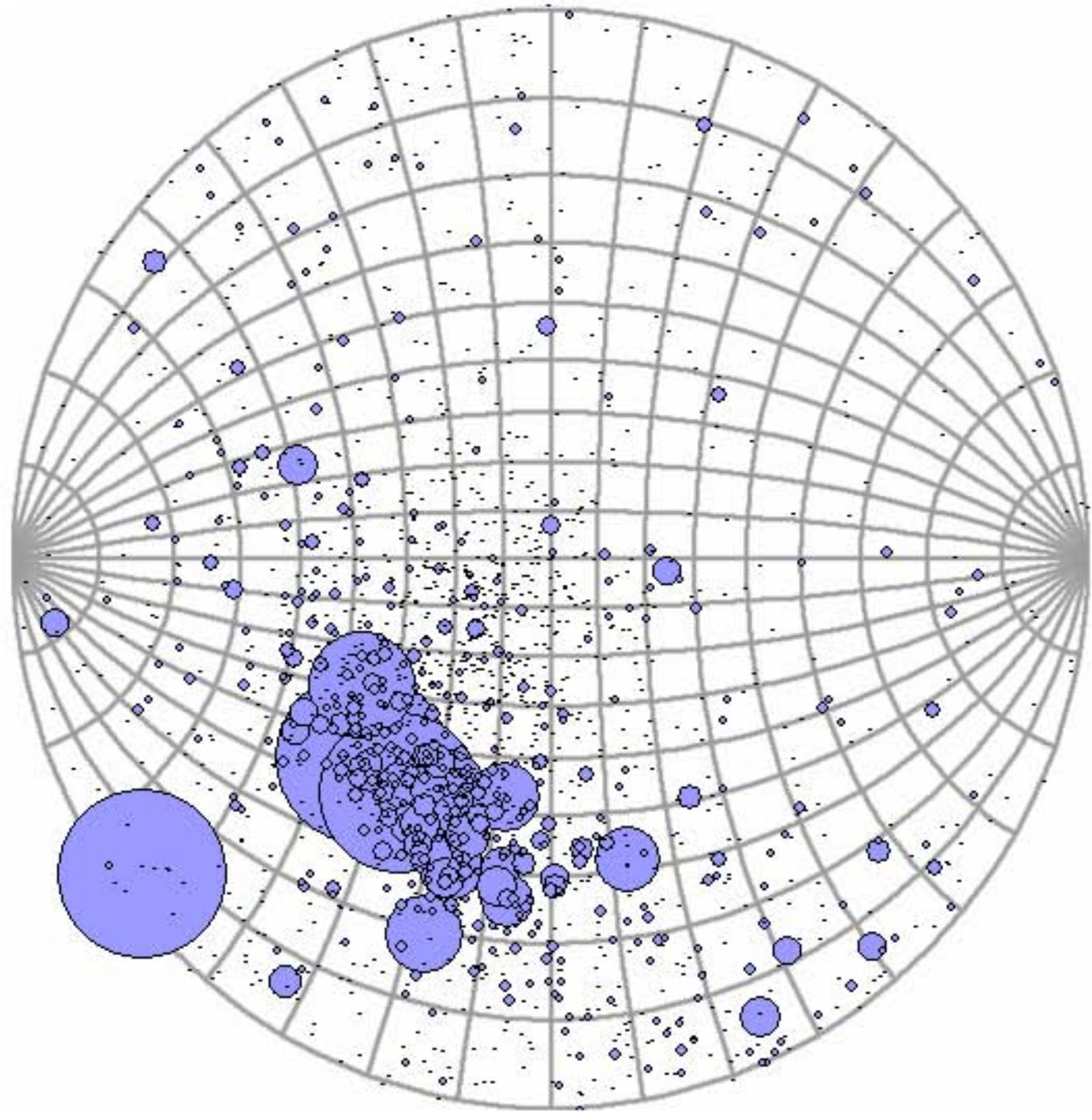


Figure 3

Vesicle long axes



Metal-sulfide contacts

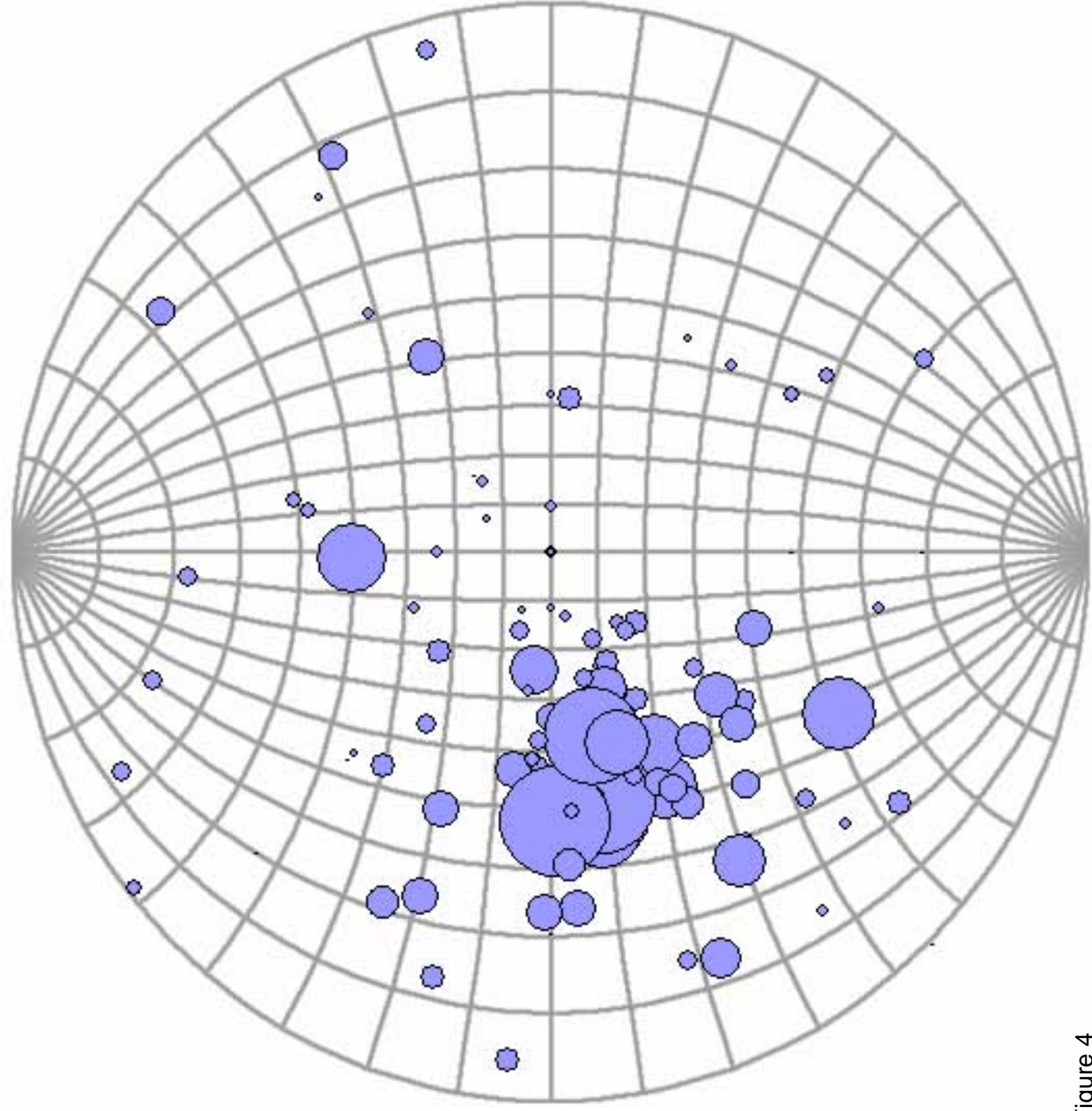


Figure 4

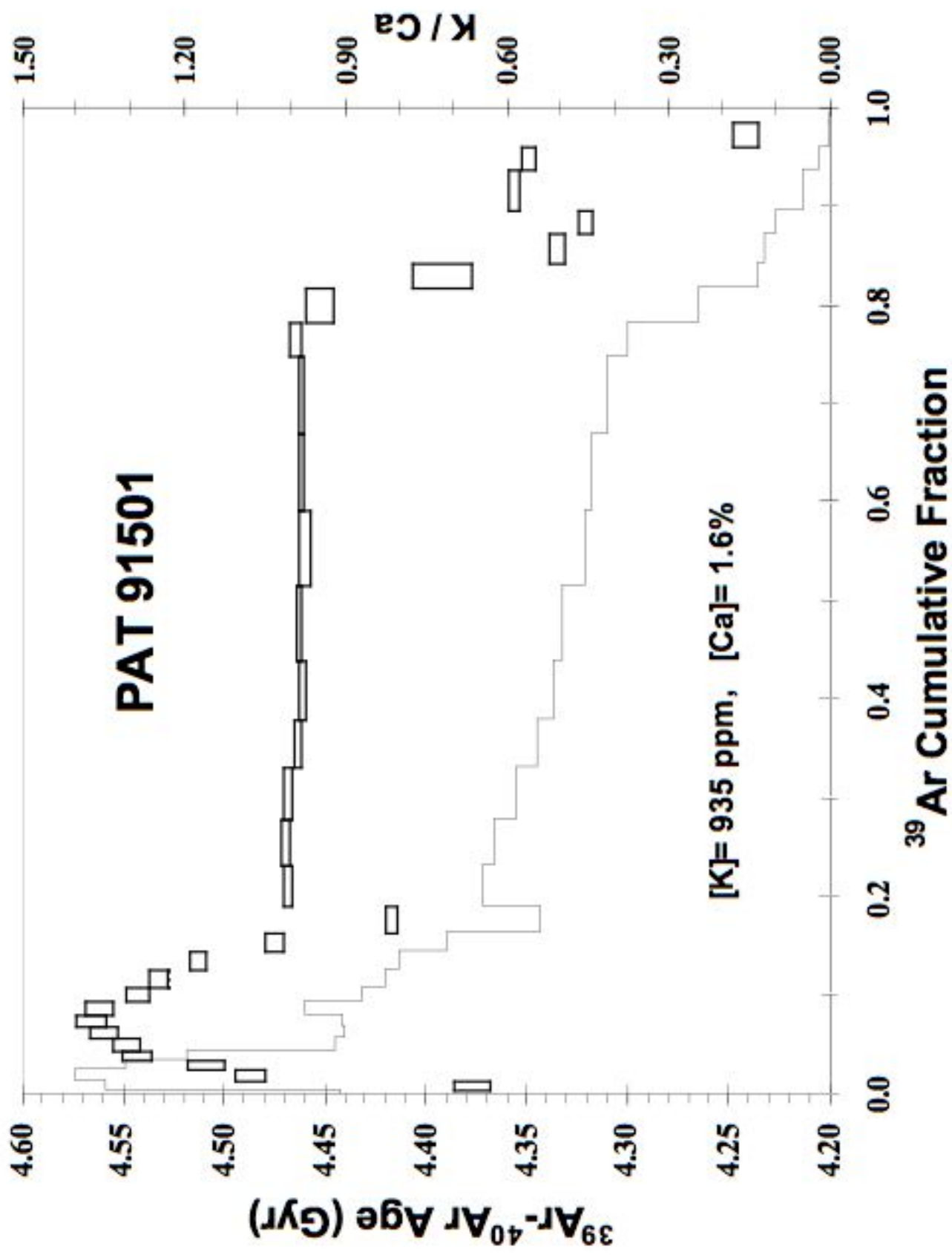


Figure 5